

Article

Geochronology and Geochemistry of the Uhelchulu Quartz Diorite-Granodiorite in Inner Mongolia of China: Implications for Evolution of the Hegenshan Ocean in the Early-Middle Devonian

Tianshe Cheng ¹, Wenjing Yang ^{2,*}, Chao Teng ¹, Xinjie Yang ¹ and Deng Xiao ¹ 

¹ Cores and Samples Center of Natural Resources, China Geological Survey, Sanhe 065201, China; chengtianshe515@163.com (T.C.); tc.1985@163.com (C.T.); yxinjie@mail.cgs.gov.cn (X.Y.); xiaodeng@mail.cgs.gov.cn (D.X.)

² Tianjin Institute of Geological Survey, Tianjin 300191, China

* Correspondence: yangwenjing515@163.com

Abstract: The Uhelchulu quartz diorite-granodiorite intrusions in Xiwuqi, Inner Mongolia, are exposed along the northwestern margin of the Xilinhot microcontinental block, located within the central and eastern parts of the southeastern Hegenshan suture zone. LA-ICP-MS zircon U-Pb dating yielded crystallization ages of (396 ± 8) Ma for the quartz diorite and (385 ± 5) Ma for the granodiorite, indicating an Early-Middle Devonian magmatic event. The quartz diorite exhibits I-type granite features, characterized by elevated Al_2O_3 (14.33–15.43 wt%), MgO (3.73–5.62 wt%), and Na ($\text{Na}_2\text{O}/\text{K}_2\text{O} = 1.04\text{--}1.44$), coupled with low P_2O_5 (0.15–0.20 wt%) and TiO_2 (0.73–0.99 wt%). Trace element patterns show relative enrichments in Rb, Th, U, and Pb, while Nb, Ta, Sr and Ti are relatively depleted. Total REE contents are relatively low (123–178 ppm), with significant LREE enrichment ($\Sigma\text{LREE}/\Sigma\text{HREE} = 4.75\text{--}5.20$), and a non-obvious Eu anomaly ($\delta\text{Eu} = 0.75\text{--}0.84$). In contrast, the granodiorite displays S-type granite characteristics, with high SiO_2 (70.48–73.01 wt%), K ($\text{K}_2\text{O}/\text{Na}_2\text{O} = 1.35\text{--}1.83$), Al_2O_3 ($\text{A}/\text{CNK} = 1.16\text{--}1.31$), and a high differentiation index ($\text{DI} = 76\text{--}82$). Notably, MgO (1.44–2.24 wt%) contents are low, and significant depletions of Ba, Sr, Ti, and Eu are observed, while Rb, Pb, Th, U, Zr, and Hf are significantly enriched. Total REE contents are relatively low (178–314 ppm), exhibiting significant LREE enrichment ($\text{LREE}/\text{HREE} = 6.17\text{--}8.36$) and a pronounced negative Eu anomaly ($\delta\text{Eu} = 0.34\text{--}0.49$). The overall characteristics point towards an active continental margin arc background for the Uhelchulu intrusions. Previous studies have suggested that the Hegenshan ocean continuously subducted northward from the Early Carboniferous to the Late Permian, but there is a lack of evidence for its geological evolution during the pre-Early Carboniferous. Therefore, this paper provides a certain basis for studying the geological evolution during the pre-Early Carboniferous in the Hegenshan ocean. We preliminarily believed that the Hegenshan ocean underwent a southward subduction towards the Xilinhot microcontinental block in the Xiwuqi area, at least from the Early Devonian to the Middle Devonian and the Hegenshan ocean may have undergone a shift in subduction mechanism during the Late Devonian or Early Carboniferous.

Keywords: Hegenshan ocean; Hegenshan suture zone; Xilinhot microcontinental block; active continental marginal arc; I-S type granite; Early-Middle Devonian; Xiwuqi



Citation: Cheng, T.; Yang, W.; Teng, C.; Yang, X.; Xiao, D. Geochronology and Geochemistry of the Uhelchulu Quartz Diorite-Granodiorite in Inner Mongolia of China: Implications for Evolution of the Hegenshan Ocean in the Early-Middle Devonian. *Minerals* **2024**, *14*, 835. <https://doi.org/10.3390/min14080835>

Academic Editor: Harald G. Dill

Received: 12 July 2024

Revised: 11 August 2024

Accepted: 13 August 2024

Published: 17 August 2024



Copyright: © 2024 by the authors. Licensee MDPI, Basel, Switzerland. This article is an open access article distributed under the terms and conditions of the Creative Commons Attribution (CC BY) license (<https://creativecommons.org/licenses/by/4.0/>).

1. Introduction

The Central Asian orogenic belt is a typical accretion-type orogenic belt located between the Eastern European Craton, Siberian Craton, Tarim Craton, and North China Craton (Figure 1a) [1–5]. Previous studies have shown that multi-ocean basins, multi-subduction zones, and multi-directional convergence are important mechanisms for continental accretion in this belt [6,7]. It is characterized by extensive accretion and collage of

continental and oceanic crustal fragments, accretionary complexes, magmatic arcs, ophiolites and other geological bodies [8,9]. From the Paleozoic to the Mesozoic, this belt experienced complex tectonic history marked by the closure of the several Paleo-Asian oceanic branches (including the Hegenshan, Okhotsk, and Solonker oceanic basin) and collage of a number of continental fragments (such as Xilinhote microcontinental block, Xing'an block) and intra-oceanic arcs to the North China Craton [10–19], with the formation of suture zones such as Hegenshan, Diyanmiao, and Solonker (Figure 1b). The Hegenshan suture zone, specifically, emerged in the eastern-northern portion of the Central Asian orogenic belt through subduction and collision processes involving the Xing'an block and Xilinhote microcontinental block [20–27].

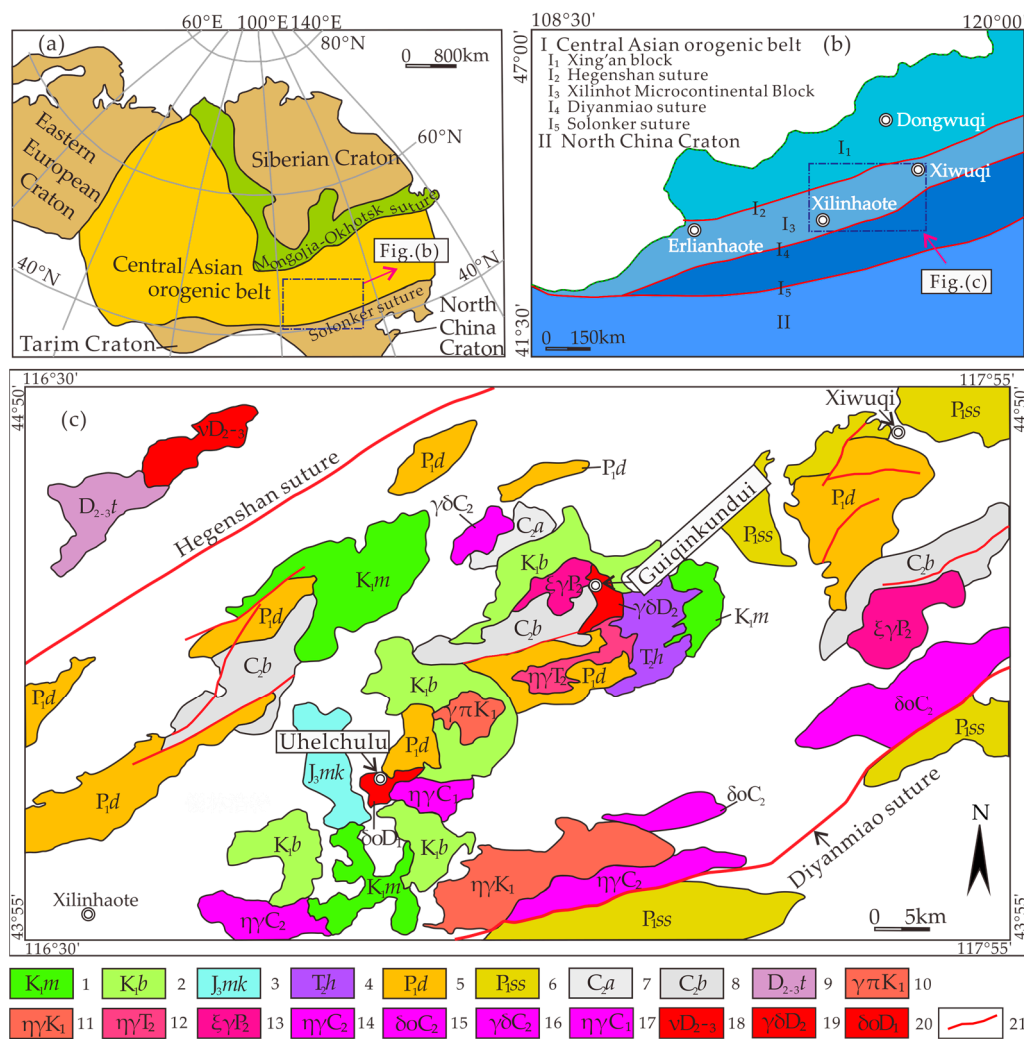


Figure 1. Tectonic division of the Central Asian orogenic belt and location of study area (a) revised after Sengör et al., 1993 [1]; Kai-Jun Zhang, 2014 [8]. (b,c) after Wang et al., 2020 [28]. 1. Cretaceous Meiletu Formation; 2. Cretaceous Baiyin Gaolao Formation; 3. Jurassic Manketu Ebo Formation; 4. Triassic Hongqi Formation; 5. Permian Dashizhai Formation; 6. Permian Shoushangou Formation; 7. Carboniferous Amushan Formation; 8. Carboniferous Ben Batu Formation; 9. Devonian Tarbagate Formation; 10. Cretaceous granite porphyry; 11. Cretaceous monzogranite; 12. Triassic monzogranite; 13. Permian syenite granite; 14. Carboniferous monzogranite; 15. Carboniferous diorite granite; 16. Carboniferous quartz diorite; 17. Carboniferous monzogranite; 18. Devonian gabbro; 19. Devonian granodiorite; 20. Devonian quartz diorite; and 21. Fracture.

Recent regional geological surveys in the Xiwuqi area of Inner Mongolia have identified numerous Carboniferous-Permian magmatic rocks, providing a valuable dataset for

understanding the tectonic evolution of the Hegenshan ocean during this period. These magmatic rocks offer insights into distinct stages of tectonic activity within this region. The pre-arc basalt in Dahat, located on the west side of the Diyanmiao ophiolite belt in Xiwuqi, as identified by Li et al., suggests the Hegenshan ocean underwent initial intra-oceanic subduction and oceanic-continental magmatism during Early Carboniferous [29]. Wang et al. discovered adakite, high magnesium andesite, and tonalite in Meilaotuola and believed that the Hegenshan ocean underwent oceanic subduction and island arc magmatism during the Late Carboniferous in Xiwuqi [30–32]. Yang et al. suggested that the gabbro-granite in Houtoumiao, Xiwuqi was formed in the subduction background of the Hegenshan ocean in Late Carboniferous [33]. The volcanic rocks in the Dashizhai Formation in the Hanwula area of Xiwuqi, as proposed by Zhang et al. originated from a post-arc spreading environment within the Hegenshan ocean in Early Permian [34,35]. The granites in Xiwuqi, such as Serbeng and Nuheting Sala, according to Fan et al. are related to the northward subduction of the Hegenshan ocean during Late Permian [36]. The above studies all suggested that the Hegenshan ocean had undergone northward subduction during the Carboniferous to Permian, which is consistent with the research results of other regions in this area, including the Early Carboniferous volcanic rocks in the Engerynpeng area of northern Suzuoqi [37], the Late Carboniferous amphibolite gabbro in Dongwuqi [38], and the Early-Late Carboniferous diorite-quartz diorite-tonalite-granodiorite in the Suzuoqi-Xiwuqi area [39].

However, the understanding of the tectonic background of the Hegenshan ocean before the Carboniferous is still unclear. Currently, only a few magmatic rocks have been identified from the Devonian in this area. Niu et al. proposed that the Hegenshan ocean was already in a post-collision extensional background during the Early Devonian based on their analysis of Huangheshao syenite in Damaoqi [40]. Huang's research on the Hegenshan ophiolite suggested that the Hegenshan ocean opened during the Middle Devonian and subsequently subducted southward during the Late Devonian, leading to collision [41–44]. Therefore, in regional geological surveys, we always hope to identify more pre-Carboniferous magmatic rocks and continuously supplement our understanding of the pre-Carboniferous geological evolution in the Hegenshan ocean.

Our study reports the first discovery of intrusive rocks from the Devonian in the Uhelchulu to Guiqinkundui areas of Xiwuqi, offering a valuable opportunity to investigate the tectonic background of the Hegenshan ocean in the Devonian. By conducting zircon U-Pb precise dating and whole-rock geochemical analyses of Uhelchulu quartz diorite and Guiqinkundui granodiorite, this paper aims to shed light on the Devonian tectonic background of the Hegenshan ocean and provide a window for a systematic study of its tectonic evolution.

2. Regional Geological Background and Petrological Characteristics

The research area is situated within the northwestern edge of the Xilinhote microcontinental block, characterized by its proximity to the south of the Hegenshan suture zone (Figure 1c) [28]. The geological evolution of the research area is closely related to the subduction process associated with the closure of the Hegenshan ocean. This tectonic activity has resulted in a distinctive structural pattern, with geological units aligning along a NE-SW trend, parallel to the extension direction of the Hegenshan suture zone (Figure 1c) [28]. The Hegenshan suture zone acts as a prominent tectonic boundary, separating distinct stratigraphic sequences on either side. On the northwestern edge of the suture, the Devonian geological bodies are the main units, dominated by the marine Tarbagate Formation and intrusions. In contrast, on the southeastern edge of the suture, within the Xilinhote microcontinental block, the geological bodies are more diverse, the stratas include the Carboniferous marine Benbatu Formation, Amushan Formation, the Permian marine-continental Shoushankou Formation, Dashizhai Formation, Zhesi Formation, the Triassic continental Hongqi Formation, and the Jurassic-Cretaceous continental volcanic rocks. The intrusive rocks include gabbro, quartz diorite, granodiorite, tonalite, and diorite from the

Carboniferous-Triassic, as well as diorite and granite porphyry from the Jurassic Cretaceous. Prior to our study, no Devonian intrusions have been found within the research area.

The Uhelchulu quartz diorite and Guiqinkundui granodiorite distribute in the prominent northeast-trending belt (Figure 1c). Quartz diorite, located in the southwestern Uhelchulu area, exhibits unconformable contacts with the overlying Lower Permian Dashizhai Formation to the north and the Lower Cretaceous Baiyingolao Formation volcanic rocks to the east. The southern margin of the quartz diorite is intruded by Early Carboniferous monzogranite. The Guiqinkundui granodiorite is overlain unconformably by the Lower Cretaceous Baiyingolao Formation volcanic rocks, the Triassic Hongqi Formation to the northeast and the Upper Carboniferous Benbatu Formation to the west and intruded by Late Triassic monzogranite to the north.

3. Sampling and Analytical Methods

3.1. Sampling

Eight samples were collected from fresh outcrops of the Uhelchulu quartz diorite and Guiqinkundui granodiorite to investigate their petrographic, geochemical, and geochronological characteristics. Among them, four samples from the Uhelchulu quartz diorite (A01, A02, A03, and A04) were selected for petrographic and whole-rock geochemical analyses, while one sample (U01) was collected for zircon U-Pb geochronology. Similarly, four samples from the Guiqinkundui granodiorite (A05, A06, A07, A08) were selected for petrographic and whole-rock geochemical analyses, with one sample (U02) selected for zircon U-Pb geochronology.

3.2. Analytical Techniques

Whole-rock geochemical analyses were carried out at the laboratory of the Regional Geological and Mineral Survey and Research Institute of Hebei Province. Major element analyses were performed using X-ray fluorescence (XRF) with an error margin of less than 2 wt%. Trace element analyses were conducted using inductively coupled plasma mass spectrometry (ICP-MS) with an accuracy exceeding 5 wt%.

Zircon grains were isolated from the rock samples through a meticulous single mineral separation process, completed with assistance from the Hebei Provincial Institute of Regional Geology and Mineral Investigation. Subsequently, cathodoluminescence (CL) imaging was performed using a scanning electron microscope at the laboratory of the Institute of Geology and Geophysics, Chinese Academy of Sciences.

Zircon U-Pb isotopic dating was conducted using LA-ICP-MS analysis at the Tianjin Geological Survey Center of the China Geological Survey. The laser ablation system employed was a UP193FX 193nm ArF excimer system (NewWave, USA, Washington), equipped with a laser from ATL (Germany, Munich) and an Agilent 7500a mass spectrometer for ICP-MS. The laser system operated at a wavelength of 193 nm with a pulse width of less than 4 ns. The laser spot diameter used for analysis was 35 μm . For external matrix correction, the internationally recognized Plesovice ($^{206}\text{Pb}/^{238}\text{U}$ weighted average age (337.13 ± 0.37) Ma) and Qinghu standard zircons ($^{206}\text{Pb}/^{238}\text{U}$ weighted average age (159.45 ± 0.16) Ma) were utilized. NIST SRM 612 with 29Si served as the internal standard element. Isotopic ratios and elemental content were calculated using the GLITTER-ver 4.0 program (Macquarie University). Ordinary lead correction was performed using Anderson's ComPbCorr # 3.17 correction program [45]. U-Pb concordia plots, age distribution frequency plots, and age weighted averages were generated using the IsoPlot/Ex_ver 3 program [46]. Detailed descriptions of the analytical methods and data processing procedures can be found in Liu et al. [47–49].

4. Results

4.1. Mineralogical Characteristics

4.1.1. Uhelchulu Quartz Diorite

The outcrop of the Uhelchulu quartz diorite is exposed in a steep slope (Figure 2a,b), and under the microscope, it presents a medium-to-fine idiomorphic crystal. Its microstructure is shown in Figure 2e, and the main minerals are plagioclase, quartz, hornblende, and biotite. Plagioclase is in a hypidiomorphic platy-shaped crystal, with faintly visible bands and double crystal development, with an abundance of 50 vol% in the rock; Quartz is xenomorphic, with an abundance of 20 vol% in the rock, occupying gaps between feldspars; Biotite occurs as sheets and has an abundance of about 10 vol% in the rock; Hornblende appears as a hypidiomorphic columnar (Figure 2e), with an abundance of about 10 vol% in the rock; and Opaque minerals are in a hypidiomorphic-to-heteromorphic granular-shaped crystal, with an abundance of <1 vol% in the rock and scattered distribution. The secondary minerals are mainly apatite and zircon.

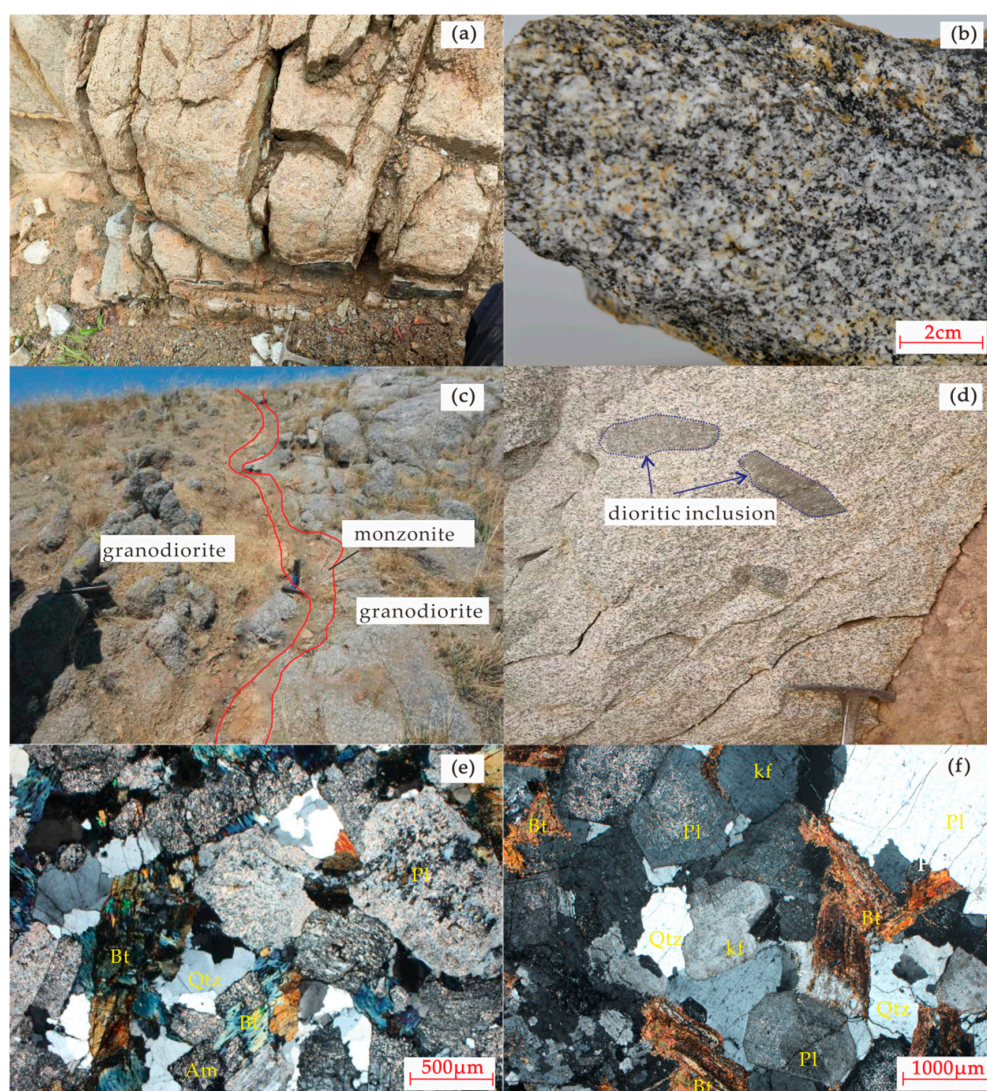


Figure 2. Field and microscopic photographs of the quartz diorite in Uhelchulu and granodiorite in Guiqinkundui. (a,b) field photos of Uhelchulu quartz diorite; (c,d) field photos of Guiqinkundui granodiorite; (e) Uhelchulu quartz diorite with hypidiomorphic crystal (crossed polarizers); (f) Guiqinkundui granodiorite hypidiomorphic crystal (crossed polarizers).

4.1.2. Guiqinkundui Granodiorite

The outcrop of the Guiqinkundui granodiorite is well exposed (Figure 2c,d). Under the microscope, it presents a fine-grained hypidiomorphic structure, fragmented patchy structure, and block-like structure. Its microstructure is shown in Figure 2f, and the main minerals are plagioclase, k-feldspar, quartz, biotite, and hornblende. Plagioclase is in hypidiomorphic platy crystal, with an abundance of 55 vol% in the rock; k-feldspar is hypidiomorphic with an interstitial distribution, with an abundance of 10 vol% in the rock; Quartz is xenomorphic, distributed between feldspars in an interstitial manner, it exhibits slight fragmentation, wavy extinction, deformation patterns, and other stress phenomena, with an abundance of 20 vol% in the rock; Biotite is flaky, with an abundance of 15 vol% in the rock. The hornblende is hypidiomorphic with a relatively low abundance in the rock.

A fine-grained biotite diorite xenolith is observed within the rock (Figure 2d), with an unclear boundary to the medium-to-fine grained granodiorite. It is mainly composed of plagioclase and biotite. The auxiliary mineral are mainly opaque minerals (<1 vol%), ilmenite, magnetite, apatite, zircon, and monazite.

From the relationship within biotite, alkali feldspar, and quartz, it can be preliminarily determined that biotite formed earlier than alkali feldspar and quartz, and the Guiqinkundui granodiorite might have undergone a strong crystallization-differentiation process. The diorite xenolith suggests that magma of the Guiqinkundui granodiorite may originate from partial melting of dioritic rocks.

4.2. Geochronology

Zircon grains extracted from the Uhelchulu quartz diorite and Guiqinkundui granodiorite exhibit a characteristic pink-yellow color and display well-defined morphologies, predominantly prismatic to short prismatic shaped crystal. The grains range in size from approximately 205 to 330 μm in length and 20 to 96 μm in width, with aspect ratios varying between 2:1 and 3:1. Cathodoluminescence (CL) imaging reveals the presence of oscillatory zoning patterns within the zircon (Figure 3a,b), indicative of a magmatic origin. These patterns are characterized by distinct rhythmic zoning structures with minimal visible residual cores. Secondary fractures are relatively limited, and the Th/U ratios of the zircon consistently exceed 0.1 (Th/U = 0.12–0.96), further corroborating a magmatic origin for the zircon grains. The results of LA-ICP-MS zircon U-Pb dating for the Uhelchulu quartz diorite and Guiqinkundui granodiorite are shown in Tables 1 and 2, respectively.

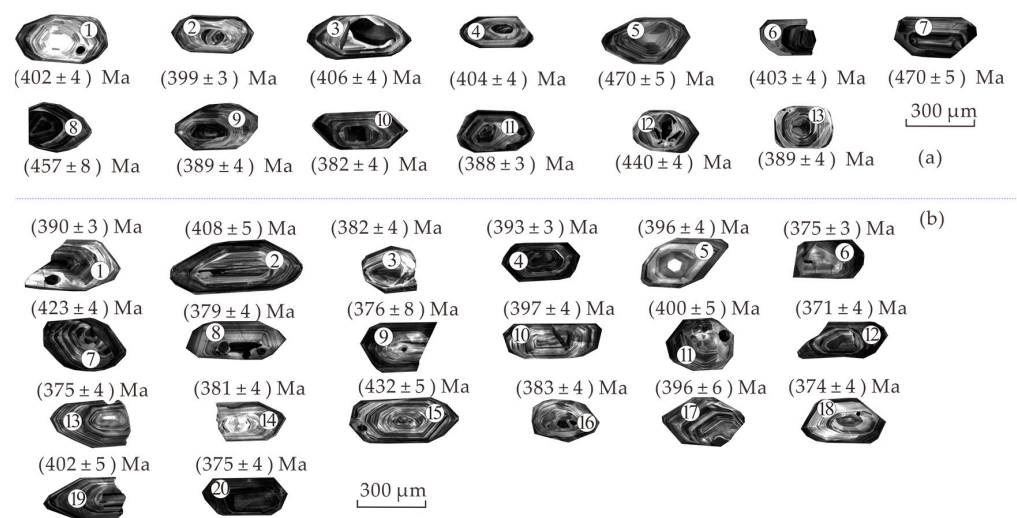


Figure 3. Cathodoluminescence (CL) images and analysis points of zircons from the Uhelchulu quartz diorite (a) and the Guiqinkundui granodiorite (b).

Table 1. LA-ICP-MS zircon U-Pb dating of the Uhelchulu quartz diorite (U01).

Spot	Content ($\times 10^{-6}$)				Isotope Ratio						Age (Ma)					
	Pb	Th	U	$^{206}\text{Pb}/^{238}\text{U}$	1σ	$^{207}\text{Pb}/^{235}\text{U}$	1σ	$^{207}\text{Pb}/^{206}\text{Pb}$	1σ	$^{232}\text{Th}/^{238}\text{U}$	$^{206}\text{Pb}/^{238}\text{U}$	1σ	$^{207}\text{Pb}/^{235}\text{U}$	1σ	$^{207}\text{Pb}/^{206}\text{Pb}$	1σ
1	9	55	136	0.0643	0.0007	0.4792	0.0136	0.0540	0.0015	0.41	402	4	398	11	371	63
2	17	70	272	0.0638	0.0005	0.4936	0.0083	0.0561	0.0009	0.26	399	3	407	7	457	36
3	15	40	237	0.0649	0.0007	0.5159	0.0091	0.0559	0.0010	0.17	406	4	422	7	447	38
4	18	69	277	0.0647	0.0006	0.5257	0.0095	0.0572	0.0010	0.25	404	4	429	8	498	39
5	16	97	198	0.0757	0.0008	0.6044	0.0134	0.0579	0.0013	0.50	470	5	480	11	527	48
6	11	87	154	0.0645	0.0006	0.5007	0.0198	0.0563	0.0021	0.58	403	4	412	16	463	84
7	14	40	158	0.0757	0.0008	0.5950	0.0119	0.1278	0.0024	0.26	470	5	474	9	2068	33
8	5	31	62	0.0735	0.0013	0.8845	0.0606	0.0867	0.0059	0.52	457	8	643	44	1355	131
9	19	104	281	0.0622	0.0006	0.6960	0.0111	0.0811	0.0013	0.38	389	4	536	9	1225	31
10	18	116	286	0.0610	0.0006	0.4551	0.0087	0.0541	0.0010	0.42	382	4	381	7	375	42
11	23	182	351	0.0621	0.0005	0.4628	0.0077	0.0541	0.0009	0.53	388	3	386	6	374	37
12	23	135	307	0.0707	0.0006	0.5431	0.0090	0.0557	0.0009	0.45	440	3	440	7	442	36
13	12	73	183	0.0622	0.0007	0.4835	0.0153	0.0563	0.0017	0.41	389	4	400	13	466	68

Tested by Tianjin Geological Survey Center of China Geological Survey.

Table 2. LA-ICP-MS Zircon U-Pb dating of the Guiqinkundui granodiorite (U02).

Spot	Content ($\times 10^{-6}$)				Isotope Ratio						Age (Ma)					
	Pb	Th	U	$^{206}\text{Pb}/^{238}\text{U}$	1σ	$^{207}\text{Pb}/^{235}\text{U}$	1σ	$^{207}\text{Pb}/^{206}\text{Pb}$	1σ	$^{232}\text{Th}/^{238}\text{U}$	$^{206}\text{Pb}/^{238}\text{U}$	1σ	$^{207}\text{Pb}/^{235}\text{U}$	1σ	$^{207}\text{Pb}/^{206}\text{Pb}$	1σ
1	33	204	516	0.0624	0.0006	0.5424	0.0163	0.0630	0.0018	0.41	390	4	440	13	709	62
2	29	55	462	0.0654	0.0009	0.5113	0.0128	0.0567	0.0015	0.12	408	5	419	11	481	59
3	15	45	248	0.0610	0.0007	0.5133	0.0236	0.0610	0.0027	0.19	382	4	421	19	640	96
4	48	128	778	0.0629	0.0006	0.5356	0.0103	0.0618	0.0011	0.17	393	4	436	8	667	38
5	31	186	449	0.0634	0.0006	0.5654	0.0116	0.0647	0.0013	0.42	396	4	455	9	764	42
6	28	122	472	0.0599	0.0005	0.4604	0.0112	0.0557	0.0013	0.27	375	3	385	9	440	54
7	24	162	329	0.0678	0.0007	0.5284	0.0182	0.0565	0.0019	0.51	423	4	431	15	472	76
8	23	117	365	0.0605	0.0006	0.5041	0.0136	0.0604	0.0017	0.33	379	4	414	11	618	60
9	19	61	303	0.0600	0.0012	0.5227	0.0403	0.0632	0.0043	0.21	376	8	427	33	714	143
10	30	100	481	0.0636	0.0006	0.5001	0.0174	0.0570	0.0019	0.21	397	4	412	14	493	75
11	59	834	888	0.0640	0.0008	0.5034	0.0082	0.0571	0.0010	0.96	400	5	414	7	495	39
12	49	212	827	0.0593	0.0007	0.4424	0.0080	0.0541	0.0010	0.26	371	4	372	7	376	43
13	20	138	321	0.0598	0.0006	0.4556	0.0167	0.0552	0.0020	0.44	375	4	381	14	421	81
14	19	118	297	0.0608	0.0006	0.4560	0.0178	0.0544	0.0020	0.41	381	4	382	15	386	84
15	32	245	410	0.0692	0.0007	0.5485	0.0176	0.0575	0.0019	0.61	432	5	444	14	509	74
16	38	158	614	0.0612	0.0006	0.4543	0.0132	0.0538	0.0015	0.26	383	4	380	11	364	63
17	15	87	242	0.0633	0.0009	0.4780	0.0153	0.0547	0.0017	0.37	396	6	397	13	401	70
18	42	227	700	0.0597	0.0007	0.4470	0.0080	0.0543	0.0009	0.33	374	4	375	7	383	39
19	24	67	387	0.0643	0.0008	0.5039	0.0113	0.0569	0.0013	0.18	401	5	414	9	487	49
20	45	246	745	0.0599	0.0007	0.4543	0.0088	0.0550	0.0010	0.34	375	4	380	7	411	43

Tested by Tianjin Geological Survey Center of China Geological Survey.

The Uhelchulu quartz diorite exhibits a consistent $^{206}\text{Pb}/^{238}\text{U}$ age distribution across all zircon grains, with the exception of those at measurement points 5, 7, 8, and 12. These latter grains may represent inherited zircon incorporated during magmatic processes. The remaining $^{206}\text{Pb}/^{238}\text{U}$ age values range from 381 to 405 Ma, clustering along the concordia line (Figure 4a). The weighted average age of 13 $^{206}\text{Pb}/^{238}\text{U}$ measurements is (395 ± 8) Ma (MSWD = 1.4), suggesting that the Uhelchulu quartz diorite crystallized during the Early Devonian (Figure 4b). Similarly, all 20 zircon grains analyzed from the Guiqinkundui granodiorite exhibit a relatively homogeneous distribution of $^{206}\text{Pb}/^{238}\text{U}$ age values, ranging

from 371 to 431 Ma, clustering along the concordia line (Figure 4c). The weighted average age of 20 ²⁰⁶Pb/²³⁸U measurements is (384 ± 5) Ma (MSWD = 1.5) (Figure 4d), indicating that the Guiqinkundui granodiorite formed during the Middle Devonian.

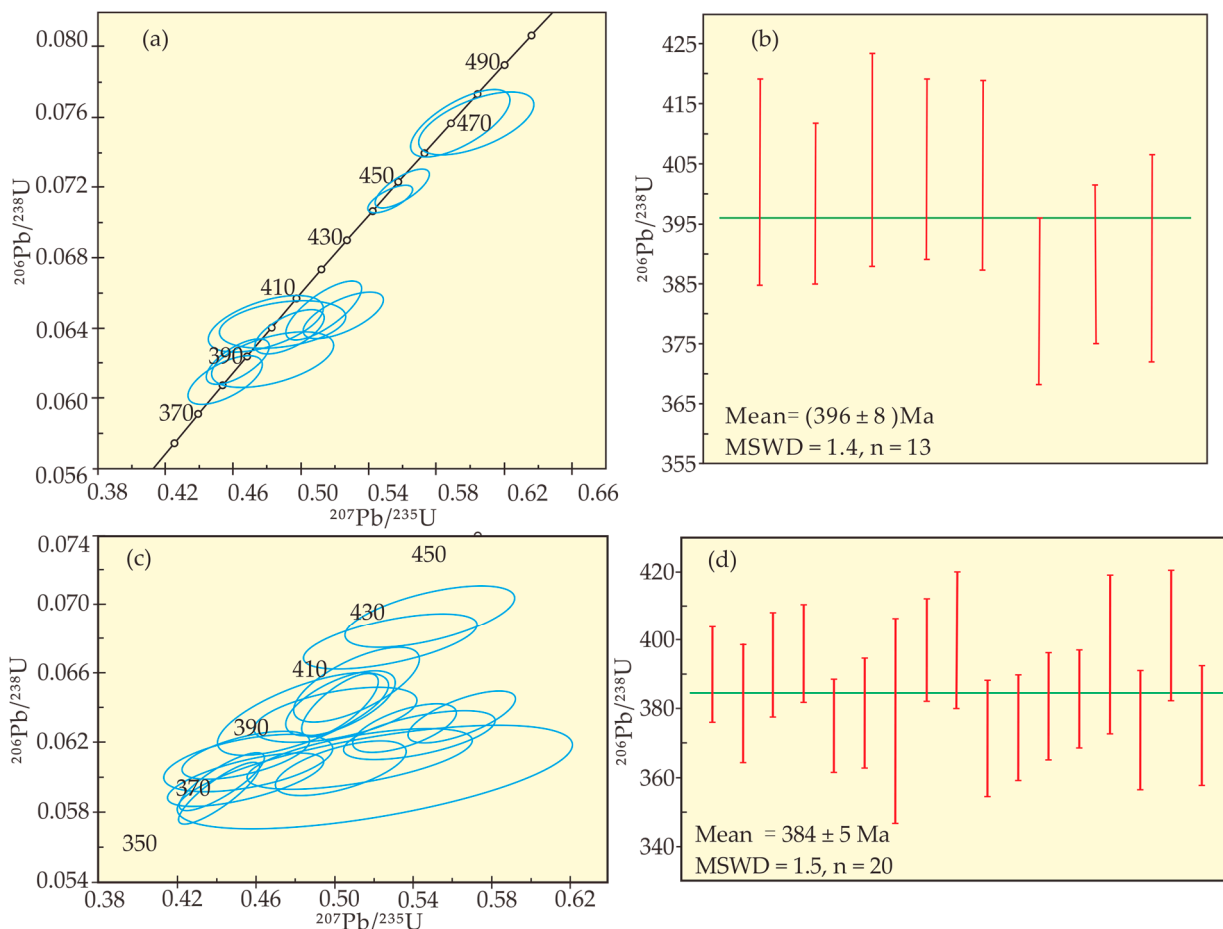


Figure 4. U-Pb concordia diagram, weighted average histogram of zircons from the Uhelchulu quartz diorite (a,b) and the Guiqinkundui granodiorite (c,d).

4.3. Whole-Rock Geochemistry

The analysis of major trace elements along with calculated normative mineral abundances (CIPW-norm) and selected geochemical ratios for the Uhelchulu quartz diorite and Guiqinkundui granodiorite, are shown in Table 3.

Table 3. Contents of major elements (wt%), trace elements (ppm), CIPW-norm of the quartz diorite in Uhelchulu and the granodiorite in Guiqinkundui.

Sample	Uhelchulu Quartz Diorite				Guiqinkundui Granodiorite			
	A01	A02	A03	A04	A05	A06	A07	A08
SiO ₂	60.44	55.71	55.39	60.53	73.01	70.48	72.27	71.04
TiO ₂	0.73	0.99	0.96	0.81	0.64	0.67	0.61	0.69
Al ₂ O ₃	14.66	15.15	15.43	14.33	11.70	12.89	13.24	12.53
Fe ₂ O ₃	1.76	2.55	2.50	2.01	0.88	0.59	0.93	0.83

Table 3. Cont.

Sample	Uhelchulu Quartz Diorite				Guiqinkundui Granodiorite			
	A01	A02	A03	A04	A05	A06	A07	A08
FeO	4.67	6.27	6.32	5.56	2.84	3.71	1.56	3.03
MnO	0.13	0.17	0.18	0.16	0.06	0.07	0.04	0.05
MgO	3.73	5.23	5.62	4.58	1.71	2.12	1.44	2.24
CaO	5.59	6.76	6.01	5.11	1.27	1.75	1.30	1.51
Na ₂ O	2.48	2.47	2.63	2.18	2.15	2.29	2.23	2.16
K ₂ O	2.39	1.72	1.87	1.77	3.94	3.10	3.75	3.47
P ₂ O ₅	0.15	0.20	0.20	0.17	0.11	0.08	0.11	0.12
LOI	3.08	2.60	2.75	2.68	1.55	2.16	1.50	1.68
Total	99.81	99.81	99.84	99.86	99.85	99.91	99.88	99.95
FeOt	6.25	8.56	8.57	7.37	3.63	4.24	2.40	3.78
FeO*/MgO	1.68	1.64	1.53	1.61	2.13	2.00	1.66	1.69
Na ₂ O/K ₂ O	1.04	1.44	1.41	1.23	0.55	0.74	0.59	0.62
A/CNK	0.87	0.83	0.89	0.97	1.16	1.25	1.31	1.24
A/NK	2.20	2.56	2.43	2.61	1.50	1.81	1.71	1.71
Ti	4359	5918	5744	4833	3813	4029	3064	3726
Y	28.2	43.3	36.3	31.0	34.1	45.9	34.5	37.3
V	170	184	199	162	76	94	72	74
Cr	119	117	154	116	50	63	49	59
Co	24.8	29.9	31.5	23.5	11.0	12.5	10.8	11.9
Ga	20.05	19.99	19.66	16.78	16.06	19.03	16.90	17.12
Rb	82.8	70.3	74.1	66.1	212.0	194.5	205.7	208.5
Sr	257	298	321	242	89	134	143	158
Ba	683	340	350	224	481	377	592	483
Zr	163	174	168	165	195	234	187	197
Nb	11.3	11.2	11.1	10.4	16.3	20.0	18.6	18.5
Hf	10.20	11.40	9.85	9.55	7.07	8.61	6.28	7.13
Ta	0.76	0.65	0.71	0.85	1.50	1.85	1.78	1.55
Pb	10.3	6.3	7.7	9.4	20.0	22.0	22.7	20.3
Th	5.16	2.94	3.96	13.81	22.01	41.22	30.88	38.17
U	0.87	0.56	0.76	0.94	3.07	2.90	2.79	3.05
La	17.97	25.47	23.72	20.05	33.02	67.62	46.37	37.49
Ce	46.51	64.36	54.91	54.14	72.66	127.08	72.3	81.4
Pr	6.08	8.89	7.28	6.06	8.12	15.97	6.21	10.17
Nd	25.38	37.91	31.07	25.48	31.36	57.60	43.11	51.22
Sm	5.53	8.49	6.97	5.87	6.65	10.86	7.85	8.91
Eu	1.46	2.01	1.75	1.42	1.03	1.19	0.88	1.07
Gd	4.88	7.48	6.28	5.15	5.98	9.09	7.98	6.72
Tb	0.89	1.37	1.16	0.96	1.11	1.51	1.32	1.36
Dy	5.82	8.98	7.53	6.34	7.17	9.13	5.21	7.15
Ho	1.14	1.74	1.49	1.22	1.35	1.83	1.40	1.53

Table 3. Cont.

Sample	Uhelchulu Quartz Diorite				Guiqinkundui Granodiorite			
	A01	A02	A03	A04	A05	A06	A07	A08
Er	3.29	5.09	4.33	3.60	3.95	5.31	3.09	4.61
Tm	0.55	0.82	0.71	0.58	0.66	0.85	0.54	0.74
Yb	3.30	4.89	4.15	3.42	4.00	5.10	3.09	4.16
Lu	0.42	0.64	0.54	0.46	0.56	0.73	0.53	0.68
δEu	0.84	0.75	0.80	0.77	0.49	0.36	0.34	0.41
(La/Yb) _N	3.67	3.51	3.85	3.96	5.57	8.94	10.12	6.08
ΣLREE	103	147	126	113	153	280	177	190
ΣHREE	20	31	26	22	25	34	23	27
ΣLREE/ΣHREE	5.07	4.75	4.80	5.20	6.17	8.36	7.63	7.06
ΣREE	123	178	152	135	178	314	2008	217
T _{Zr} (°C)	748	734	740	762	817	839	808	813
10,000 × Ga/Al	1.58	1.49	1.41	1.21	1.59	1.79	1.41	1.58
Zr + Nb + Ce + Y	249	293	270	260	318	427	270	260
Quartz(Q)	18.63	11.23	9.56	21.03	39.53	37.02	34.50	34.32
Anorthite(An)	22.54	25.93	25.52	24.81	5.64	8.34	5.82	6.83
albite(Ab)	21.7	21.46	22.91	18.94	18.53	19.82	27.75	23.77
orthoclase(Or)	14.6	10.44	11.37	10.74	23.69	18.73	22.50	20.87
diopside(Di)	4.14	5.86	3.14	0.1				
hyersthenite(Hy)	13.95	18.87	21.42	19.4	7.93	10.87	4.82	9.58
ilmenite(Il)	1.43	1.93	1.87	1.58	1.23	1.31	1.18	1.33
magnetite(Mt)	2.64	3.81	3.73	3	1.3	0.88	1.37	1.22
apatite(Ap)	0.37	0.48	0.47	0.41	0.27	0.19	0.26	0.28
corundum (C)					1.89	2.85	1.79	1.81

Note: FeO* = FeO + 0.899 × Fe₂O₃.

4.3.1. Major Elements

The Uhelchulu quartz diorite exhibits SiO₂ ranging from 55.39 to 60.53 wt% (Table 3). Other major element concentrations include: Al₂O₃ (14.33–15.43 wt%), K₂O (1.77–2.39 wt%), Na₂O (2.18–2.63 wt%), TiO₂ (0.73–0.99 wt%), MnO (0.13–0.18 wt%), MgO (3.73–5.62 wt%), CaO (5.11–6.76 wt%), and P₂O₅ (0.15–0.20 wt%). The K₂O + Na₂O content varies between 3.95 and 4.87 wt%, with a Na₂O/K₂O ratio of 1.04 to 1.44. The A/CNK and A/NK ratios fall within the ranges of 0.83–0.97 and 2.20–2.61, respectively. Normative mineral calculations based on the CIPW norm reveal a quartz content ranging from 9.56 to 21.03 wt%, and an apatite content of 0.37 to 0.48 wt%, with no presence of corundum. The Uhelchulu quartz diorite is characterized by low potassium, high sodium, and high calcium content, along with relatively low concentrations of TiO₂, MnO, and P₂O₅. This geochemical signature is consistent with a rock that has undergone significant fractional crystallization. In the TAS diagram (Figure 5a) [50], the sample points fall within the diorite-gabbro diorite field. The AFM diagram (Figure 5b) [51] indicates that the Uhelchulu quartz diorite belongs to the calc-alkaline series.

The Guiqinkundui granodiorite displays a relatively high silica content, with SiO₂ ranging from 70.48 to 73.01 wt% (Table 3). The K₂O + Na₂O content ranges from 5.39 to 6.09 wt%, with K₂O concentrations ranging from 3.10 to 3.94 wt% and a K₂O/Na₂O ratio of 1.35 to 1.83. These values indicate a rock that is alkali-rich and specifically potassium-rich.

The high CaO/Na₂O ratio (0.58–0.76 > 0.3) further supports this conclusion. The Al₂O₃ content varies from 11.70 to 13.24 wt%, resulting in an A/CNK ratio of 1.16 to 1.31. The presence of corundum molecules in the CIPW norm classifies the rock as peraluminous. The CaO, MnO, P₂O₅, and TiO₂ content is relatively low, resulting in a differentiation index (DI) of 76–82. This high DI value indicates that the rock mass has undergone a significant degree of differentiation and evolution. In the TAS diagram (Figure 5a) [50], the sample points fall within the granite-granodiorite field. Similarly, the AFM diagram (Figure 5b) [51] confirms that the Guiqinkundui granodiorite belongs to the calc-alkaline series.

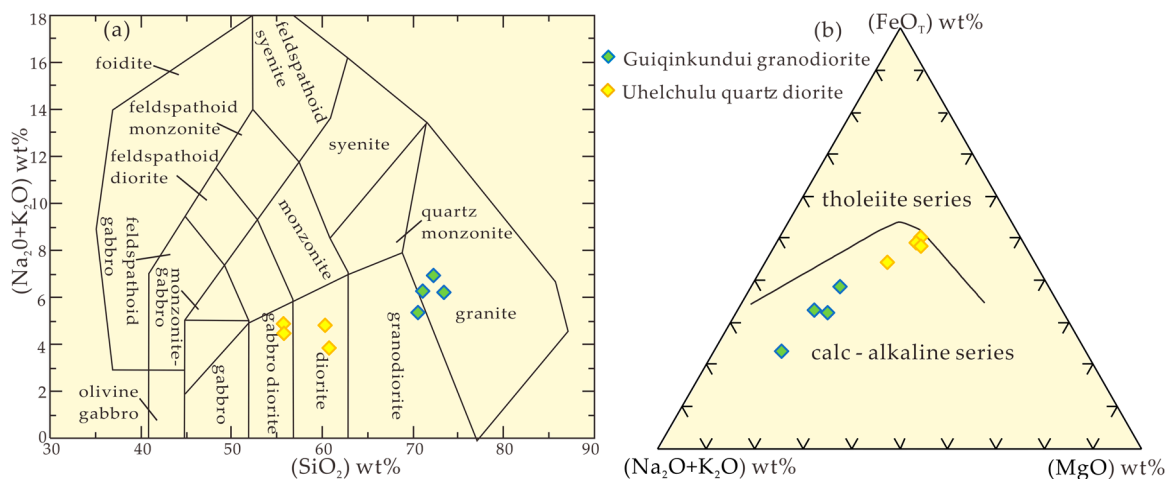


Figure 5. TAS and AFM diagram of quartz diorite-granodiorite from Uhelchulu to Guiqinkundui in Xiwuqi ((a) after E.A.K.Middlemost, 1994 [50]; (b) after Irvine T. N., et al. 1971 [51]).

4.3.2. Trace Elements

The trace element compositions of the Uhelchulu quartz diorite and Guiqinkundui granodiorite exhibit notable similarities and differences (Table 3, Figure 6a,b). Both rock types show REE patterns with significant light over heavy REE enrichment and little fractionation within the heavy REE when normalized to chondrite [52], indicative of enrichment in both light and heavy REEs with significant fractionation between the two groups.

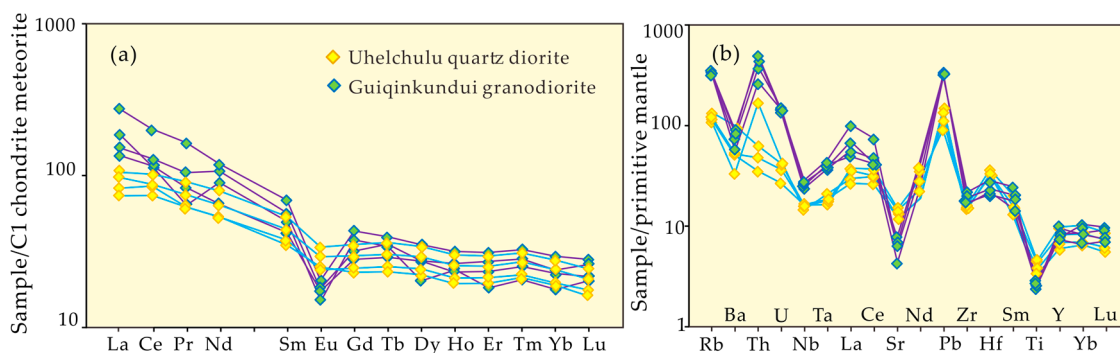


Figure 6. (a) Chondrite-normalized REE distribution patterns (after Boynton, 1984 [52]) and (b) Primitive mantle-normalized trace elements distribution patterns (after Sun and McDonough, 1989 [53]) for the Uhelchulu quartz diorite and Guiqinkundui granodiorite, Xiwuqi.

The total REE content (Σ REE) is slightly lower than it in the Uhelchulu quartz diorite (123–178 ppm) compared to the Guiqinkundui granodiorite (178–314 ppm). However, the Guiqinkundui granodiorite exhibits a more pronounced negative europium anomaly (δ Eu = 0.36–0.49) compared to the Uhelchulu quartz diorite (δ Eu = 0.75–0.84).

Overall, both rock types are characterized by elevated trace element concentrations with respect to the primitive mantle [53]. They display significant depletion of Ba, Nb, Ta,

Sr, Eu, and Ti, while Rb, Th, U, Pb, Zr, and Hf are notably enriched. The Guiqinkundui granodiorite displays more pronounced “peak” values for these elements compared to the Uhelchulu quartz diorite.

The geochemical signatures of the Uhelchulu quartz diorite and Guiqinkundui granodiorite suggest that they likely originated from similar source rocks potentially related to island arc-type magmatism. The source may have involved partial melting of lower crustal diorite rocks, followed by assimilation of crustal materials during intrusion. The Guiqinkundui granodiorite appears to have undergone more significant fractional crystallization compared to the Uhelchulu quartz diorite.

5. Discussion

5.1. Intrusion Age

Previous studies on the Uhelchulu quartz diorite and Guiqinkundui granodiorite have lacked precise geochronological constraints. The 1:200,000 Maodeng regional geological survey report by the Bureau of Inner Mongolia Geology (1976) [54] classified the Guiqinkundui granodiorite as a middle acidic intrusive rock of Late Hualixi age, corresponding to the Late Permian. Furthermore, the Institute of Inner Mongolia Autonomous Region Geological Survey (2008) [55], in their 1:250,000 Chaokewula regional geological survey report, speculated the unit to be Late Jurassic.

This study presents precise zircon U-Pb dating results, revealing ages of (396 ± 8) Ma (MSWD = 1.4) for the Uhelchulu quartz diorite and (385 ± 5) Ma (MSWD = 1.5) for the Guiqinkundui granodiorite. The measured zircons exhibit exclusively magmatic characteristics, confirming the Early Devonian and Middle Devonian ages of these intrusions, respectively. These findings contradict previous assumptions of a late Variscan or Late Jurassic origin for these rocks.

These newly determined ages significantly expand the record of tectonic-magmatic activity in the Xiwuqi area from the Carboniferous-Permian to the Devonian. This discovery provides a crucial chronological framework for investigating the tectonic evolution of the Hegenshan ocean during the Devonian period.

5.2. Petrogenesis

The petrogenesis of granitic rocks is widely understood to be governed by the source characteristics, leading to the distinction of granites into I-type, S-type, A-type, and M-type, with M-type granites being relatively uncommon [56]. A-type granites are typically distinguished by the presence of alkaline mafic minerals [57]. Chemically, A-type granites are characterized by elevated concentrations of elements like Zr, Nb, Ce, Ga, and Y, as well as high silicon, potassium, and iron. These granites are also typically associated with high crystallization temperatures [58–60].

The FeO^*/MgO ratios of the Uhelchulu quartz diorite and Guiqinkundui granodiorite (1.53–2.13) fall well below the significantly iron-rich A-type granite classification ($\text{FeO}^*/\text{MgO} > 10$) [61]. Detailed petrographic analysis revealed the absence of alkaline mafic minerals, a key characteristic of A-type granites. Furthermore, zircon saturation temperatures, determined through whole-rock major element and Zr content analysis, suggest relatively lower crystallization temperatures compared to A-type granites. The Uhelchulu quartz diorite exhibits a zircon saturation temperature range of 734–762 °C (average 746 °C; Table 3), while the Guiqinkundui granodiorite displays a range of 817–839 °C (average 819 °C; Table 3) [62]. Both of these temperature ranges fall below the average A-type granite temperature of 833 °C [62].

The Ga/Al ratio ($10,000 \times \text{Ga}/\text{Al}$) ranges from 1.21 to 1.79, significantly lower than the established A-type granite threshold of 2.6 [61]. Similarly, the sum of Zr + Nb + Ce + Y (249–427 ppm, average 303 ppm) falls below the A-type granite lower limit of 350 ppm [61] (Table 3). These geochemical observations further corroborate the notion that the Uhelchulu quartz diorite and Guiqinkundui granodiorite do not exhibit the defining petrological and

geochemical characteristics of A-type granites. Instead, their features are more consistent with those of I-type or S-type granites, as supported by relevant diagrams (Figure 7a,b) [61].

Previous studies have established that apatite solubility decreases with increasing SiO_2 during magma differentiation in metaluminous to weakly peraluminous magmas [62,63]. However, in strongly peraluminous magmas, the solubility trend is reversed. The Uhelchulu quartz diorite exhibits an extremely low P_2O_5 content (0.15–0.20 wt%) that consistently decreases with increasing SiO_2 content (Figure 7c) [64], aligning with the established evolutionary trend of I-type granites. Furthermore, the Uhelchulu quartz diorite samples plot within the I-type granite field on the Na_2O - K_2O diagram (Figure 7d). In contrast, the P_2O_5 content of the Guiqinkundui granodiorite shows a positive correlation with SiO_2 (Figure 7c) [64], and its samples fall within the S-type granite field on the Na_2O - K_2O diagram (Figure 7d) [64]. Additionally, CIPW normative mineral calculations for the Guiqinkundui granodiorite indicate the presence of corundum (1.79–2.85 vol%), confirming its peraluminous nature.

Therefore, we tentatively conclude that the Uhelchulu quartz diorite has I-type granite characteristics, while the Guiqinkundui granodiorite has S-type granite characteristics. Previous studies and experimental petrology have shown that the genesis of I-type and S-type granites is mainly due to partial melting and fractional crystallization of crustal materials [65–67].

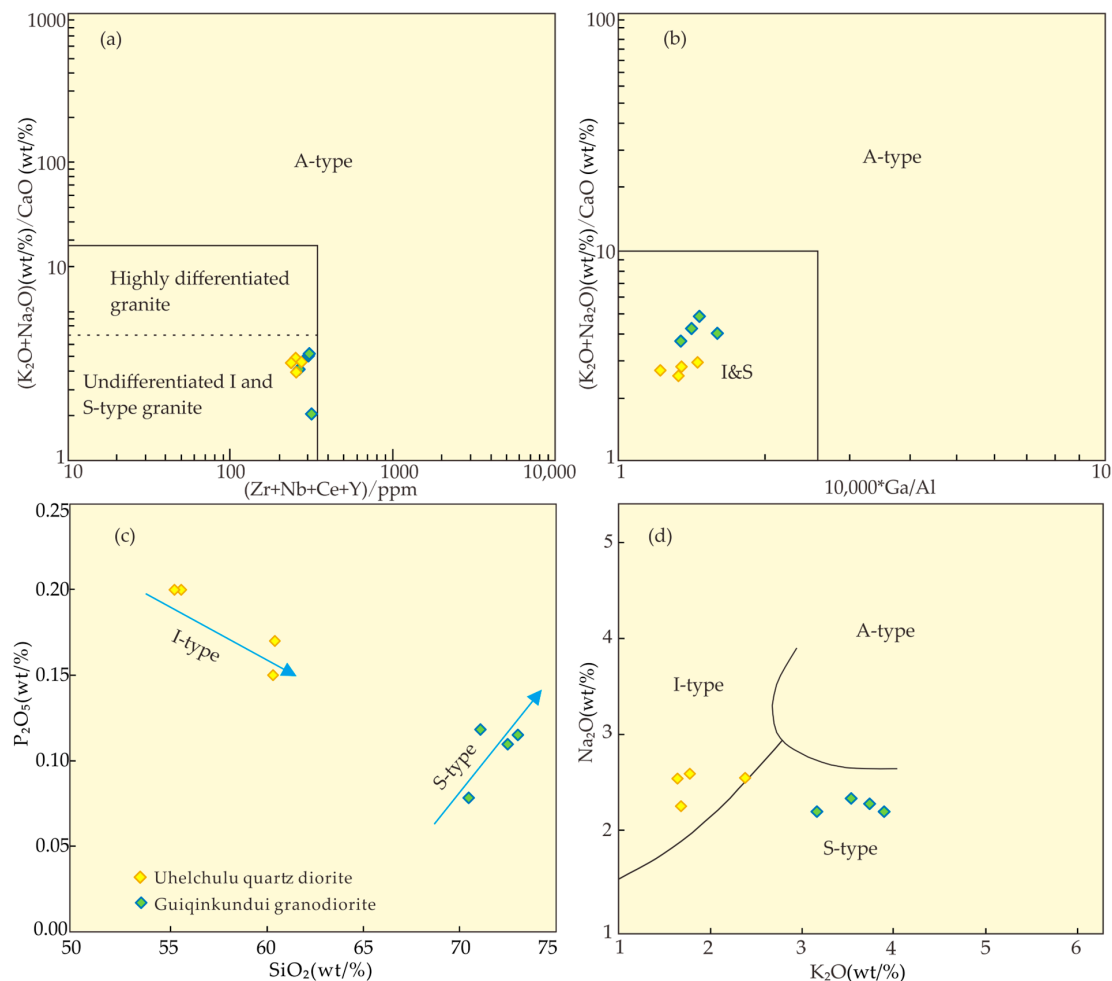


Figure 7. Geochemical discrimination diagrams for Uhelchulu quartz diorite and Guiqinkundui granodiorite samples in Xiwuqi. (a) $(\text{K}_2\text{O} + \text{Na}_2\text{O})/\text{CaO}$ versus $\text{Zr} + \text{Nb} + \text{Ce} + \text{Y}$ (ppm) (after Whalen et al., 1987 [61]); (b) $(\text{K}_2\text{O} + \text{Na}_2\text{O})/\text{CaO}$ versus $10,000 * \text{Ga}/\text{Al}$ (after Whalen et al., 1987 [61]); (c) Na_2O versus K_2O (after Collins et al., 1982 [64]); and (d) P_2O_5 versus SiO_2 (after Collins et al., 1982 [64]).

5.3. Tectonic Implications

The Devonian tectonic environment of the Hegenshan ocean remains poorly understood, primarily due to limited research and a scarcity of geological evidence. Existing interpretations of the Hegenshan ocean Devonian evolution depend largely on studies of Devonian magmatic rocks within the Hegenshan ophiolitic mélangé belt. Huang proposed that the Hegenshan ocean began forming during the Middle-Late Devonian, underwent northward subduction during the Early Carboniferous, and ultimately closed during the Late Carboniferous [41]. Shao et al. based on the age of the Gegenaobao volcanic rocks and the emplacement of ultrabasic rocks, suggested that the Hegenshan ocean closed during the Late Devonian-Early Carboniferous, with an unconformity observed between the serpentinite and the overlying strata in the Hegenshan area [68].

The first discovery of Devonian intrusive rocks in the Xiwuqi area during the regional geological survey provides valuable insights into the Devonian tectonic environment of the Hegenshan ocean. Despite the limited availability of other geological evidence from the same period, this study offers a preliminary exploration of the tectonic setting associated with the formation of the Uhelchulu quartz diorite and Guiqinkundui granodiorite, drawing primarily on their geochemical characteristics.

Using Nb-Y and Rb-(Y + Nb) discrimination diagrams (Figure 8a,b) [69], all samples of Uhelchulu quartz diorite and Guiqinkundui granodiorite plot within the volcanic arc environment. This geochemical evidence, combined with the detailed petrogenesis analysis, supports the formation of these rocks in an active continental margin arc environment, thus strongly contracting earlier interpretations, providing compelling evidence for a distinct tectonic setting during their formation.

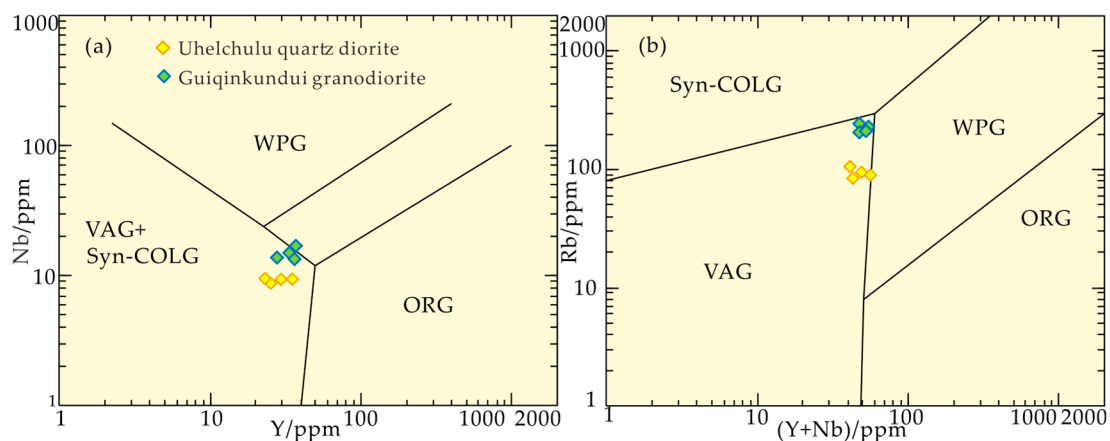


Figure 8. Discrimination diagrams for Uhelchulu quartz diorite and Guiqinkundui granodiorite in Xiwuqi, (a) Y-Nb and (b) (Y + Nb)-Rb (after Pearce et al., 1984 [69]). Syn-COLG (syn-collision granite); WPG (within plate granite); VAG (volcanic arc granite); and ORG (mid ocean ridge granite).

Petrological and geochemical analyses of the Uhelchulu quartz diorite and Guiqinkundui granodiorite indicate that the Xiwuqi area occupied an active continental margin arc setting within the Xilinhote microcontinental block during the Early to Middle Devonian. This interpretation suggests that the Hegenshan oceanic crust underwent southward subduction during this period (Figure 9a). Previous research has suggested that the Hegenshan ocean transitioned to northward subduction at least during the Early Carboniferous (Figure 9b). Therefore, we preliminarily believed that the Hegenshan ocean may have undergone a shift in subduction mechanism during the Late Devonian or Early Carboniferous.

Profeta et al. (2016) proposed a fitting relationship between the whole-rock chemistry $(La/Yb)_N$ of intrusions and crustal thickness: $H = 21.277 \ln(1.0204w(La)_N/w(Yb)_N)$, Where H is the thickness of the crust and $w(La)_N/w(Yb)_N$ is the ratio after homogenization of chondrite meteorite [70]. This calculation needs to remove the samples that do not meet

the requirements, such as $La > 1 \times 10^{-6}$, $Th/U < 0.1$, and $SiO_2 > 75\%$ in the whole-rock chemistry [71,72]. We calculated the variation in crustal thickness from the Early Devonian to Early Cretaceous in the research area (Figure 10) based on the data from this paper and other researchers (Table 4) [30,36,39,73–77]. The crustal thickness in the Early Devonian is relatively thin (~28.52 km), but it increased to 43.13 km during the Middle Devonian. The crustal thickening might continue until the Middle Carboniferous (~42.60 km), which might be related to the continuous southward subduction of the Hegenshan ocean. In the late Early Carboniferous, there was a sudden thinning of the crust, which might be related to the shift in the subduction mechanism of the Hegenshan ocean in the Early Carboniferous. This calculation result might further support the understanding of our study. Subsequently, it underwent crustal thickening and thinning processes several times until the Early Cretaceous in the research region, which is consistent with the geological evolution processes studied by previous researchers.

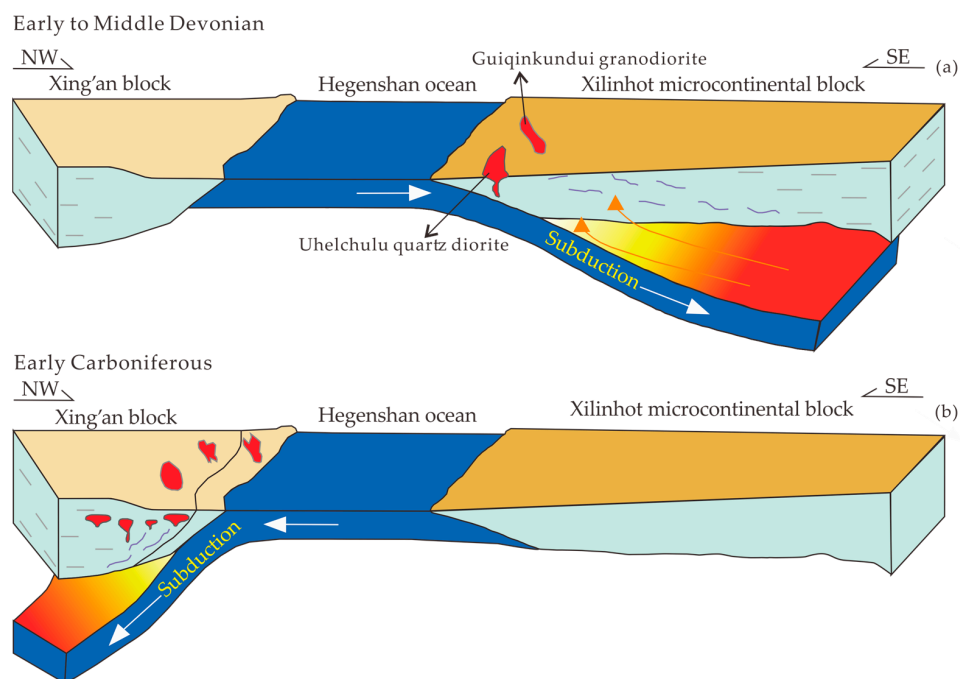


Figure 9. Tectonic evolution model of the middle-east section of the Hegenshan ocean in the Early-Middle Devonian (a) and Early Carboniferous (b).

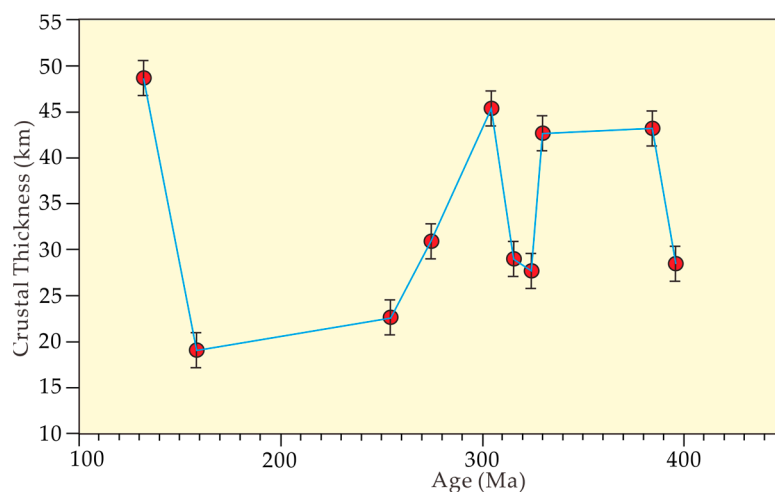


Figure 10. Crustal thickness evolution in the research area.

Table 4. The calculation results of crustal thickness in the research area.

Source	Uhelchulu Quartz Diorite				Guiqinkundui Granodiorite				[59]	[23]	[60]	[14]	[58]	[20]	[57]	[56]		
Sample	A01	A02	A03	A04	A05	A06	A07	A08	PM2	JG21	14NM	PS1-8	PS1-1	P37	SEB1	ST01	PT1	PT2
SiO ₂	60.44	55.71	55.39	60.53	73.01	70.48	72.27	71.04	66.37	54.36	51.71	66.58	67.92	74.22	65.96	74.68	60.40	63.23
Th/U	0.41	0.41	0.41	0.41	0.41	0.41	0.41	0.41	0.55	0.75	2.07	0.30	0.30	0.42	0.48	0.35	0.33	0.33
La	17.97	25.47	23.72	20.05	33.02	67.62	46.37	37.49	8.70	9.04	8.40	10.89	14.57	31.50	17.03	24.49	32.00	22.20
Yb	3.30	4.89	4.15	3.42	4.00	5.10	3.09	4.16	0.86	1.80	1.57	0.91	1.33	5.41	0.54	7.30	2.19	1.78
(La/Yb) _N	3.67	3.51	3.85	3.96	5.57	8.94	10.12	6.08	7.26	3.60	3.84	8.58	7.86	4.18	22.62	2.41	10.48	8.95
H		28.52				43.13			42.60	27.68	29.00	45.23		30.84	22.62	19.11	48.74	
Age (Ma)		396				385			330	325	316	305		275	255	159	132	

6. Conclusions

This study provides novel insights into the Devonian tectonic evolution of the Hegenshan ocean, based on the petrological and geochemical characterization of the Uhelchulu quartz diorite and Guiqinkundui granodiorite in the Xiwuqi area.

LA-ICP-MS zircon U-Pb dating yielded ages of (396 ± 8) Ma (MSWD = 1.4) for the Uhelchulu quartz diorite and (385 ± 5) Ma (MSWD = 1.5) for the Guiqinkundui granodiorite, conclusively demonstrating Early to Middle Devonian magmatic activity. This discovery significantly expands the known extent of Devonian magmatism, previously documented only north of the Hegenshan suture zone, to the southern Xiwuqi area. These ages provide critical chronological constraints for further elucidating the complex tectonic evolution of the Hegenshan ocean during this critical period.

The mineralogical and whole-rock geochemical characteristics suggest that the Uhelchulu quartz diorite has I-type granite characteristics, while the Guiqinkundui granodiorite has S-type granite characteristics.

Geochemical analysis of the tectonic environment indicated that the Uhelchulu quartz diorite and Guiqinkundui granodiorite formed in an active continental margin arc background, which may be related to the southward subduction of the Hegenshan ocean in the Early to Middle Devonian. The Hegenshan ocean might have undergone a shift in subduction mechanism during the Late Devonian or Early Carboniferous.

Author Contributions: Conceptualization, T.C., and W.Y.; methodology, T.C. and W.Y.; software, T.C., W.Y., C.T. and X.Y.; validation, T.C., W.Y. and D.X.; formal analysis, T.C. and W.Y.; investigation, T.C., W.Y., C.T. and X.Y.; resources, T.C. and W.Y.; data curation, T.C., W.Y., C.T. and X.Y.; writing—original draft preparation, T.C. and W.Y.; writing—review and editing, T.C. and W.Y.; visualization, T.C. and W.Y.; supervision, W.Y.; project administration, T.C. and W.Y.; funding acquisition, T.C. and W.Y. All authors have read and agreed to the published version of the manuscript.

Funding: This research was funded by grants from China Geological Survey (Grants [2010]01-19-01, DD20221814, DD20242250).

Data Availability Statement: The authors confirm that the data generated or analyzed during this study are provided in full within the published article.

Acknowledgments: We thank the editors and anonymous reviewers for their critical reviews and excellent suggestions that helped to improve this manuscript. We thank Xuebin Zhang and Jie Shao for their help and valuable comments. We also thank Xiqing Cheng, Jun Cao for their valuable help. We would like to express our gratitude to the leadership and staff of the Exploration Department at the Tianjin Geological Survey and Research Institute for their assistance and support with the field research.

Conflicts of Interest: All the authors declare that there is no conflict of interest regarding the publication of this article.

References

1. Sengör, A.M.C.; Natalin, B.A.; Burtman, V.S. Evolution of the Altaid tectonic collage and Palaeozoic crustal growth in Eurasia. *Nature* **1993**, *364*, 299–307. [[CrossRef](#)]
2. Xiao, W.; Song, D.; Windley, B.F.; Li, J.; Han, C.; Wan, B.; Zhang, J.; Ao, S.; Zhang, Z. Research progresses of the accretionary processes and metallogenesis of the Central Asian Orogenic Belt. *Sci. China Earth Sci.* **2019**, *63*, 329–361. [[CrossRef](#)]
3. Windley, B.F.; Allen, M.B.; Zhang, C.; Zhao, Z.Y.; Wang, G.R. Paleozoic accretion and Cenozoic redeformation of the Chinese Tian Shan range, central Asia. *Geology* **1990**, *18*, 128–131. [[CrossRef](#)]
4. Windley, B.F.; Alexeiev, D.; Xiao, W.; Kröner, A.; Badarch, G. Tectonic models for accretion of the Central Asian orogenic belt. *J. Geol. Soc.* **2007**, *164*, 31–47. [[CrossRef](#)]
5. Windley, B.F.; Xiao, W. Ridge subduction and slab windows in the Central Asian orogenic belt: Tectonic implications for the evolution of an accretionary orogen. *Gondwana Res.* **2018**, *61*, 73–87. [[CrossRef](#)]
6. Xiao, W.; Windley, B.F.; Han, C.; Liu, W.; Wan, B.; Zhang, J.; Ao, S.; Zhang, Z.; Song, D. Late Paleozoic to early Triassic multiple roll-back and oroclinal bending of the Mongolia collage in central Asia. *Earth-Sci. Rev.* **2018**, *186*, 94–128. [[CrossRef](#)]
7. Xiao, W.; Windley, B.F.; Sun, S.; Li, J.; Huang, B.; Han, C.; Yuan, C.; Sun, M.; Chen, H. A tale of amalgamation of Permo-Triassic collage systems in central Asia: Oroclines, sutures, and terminal accretion. *Annu. Rev. Earth Planet. Sci.* **2015**, *43*, 477–507. [[CrossRef](#)]

8. Zhang, K.J. Genesis of the Late Mesozoic Great Xing'an Range Large Igneous Province: A Mongol-OKhotsk slab window model. *Int. Geol. Rev.* **2014**, *56*, 1557–1583. [[CrossRef](#)]
9. Zhang, K.J.; Ji, C.; Zhou, Y.Z.; Zhang, Y.J. Tracing oceanic plateau relics in the basement of mainland China: A synthesis of aeromagnetic and seismic refraction data. *Earth-Sci. Rev.* **2024**, *255*, 104849. [[CrossRef](#)]
10. Hui, J.; Zhang, K.-J.; Zhang, J.; Qu, J.; Zhang, B.; Zhao, H.; Niu, P. Middle-late Permian high-K adakitic granitoids in the NE Alxa block, northern China: Orogenic record following the closure of the Paleo-Asian oceanic branch? *Lithos*, 1063.
11. Zhang, K.J.; Yan, L.L.; Ji, C. Switch of NE Asia from extension to contraction at the mid-Cretaceous: A tale of the Okhotsk oceanic plateau from initiation by the Perm Anomaly to extrusion in the Mongol–Okhotsk ocean? *Earth-Sci. Rev.* **2019**, *198*, 102941. [[CrossRef](#)]
12. Li, G.Z.; Wang, Y.J.; Li, C.Y. Discovery of Early Permian radiolarian fauna in the Solon Obo ophiolite belt, Inner Mongolia and its geological significance. *Chin. Sci. Bull.* **2017**, *62*, 400–406. (In Chinese) [[CrossRef](#)]
13. Liu, J.F.; Li, J.Y.; Chi, X.G.; Qu, J.F.; Hu, Z.C. A late-Carboniferous to early early-Permian subduction-accretion complex in Daqing pasture, southeastern Inner Mongolia: Evidence of northward subduction beneath the Siberian paleoplate southern margin. *Lithos* **2013**, *177*, 285–296. [[CrossRef](#)]
14. Xiao, W.J.; Windley, B.F.; Hao, J. Accretion leading to collision and the Permian Solonker suture, Inner Mongolia, China: Termination of the central Asian orogenic belt. *Tectonics* **2003**, *22*, 1069–1089. [[CrossRef](#)]
15. Zhang, Z.C.; Li, K.; Li, J.F.; Tangy, W.H.; Chen, Y.; Luo, Z.W. Geochronology and geochemistry of the eastern Erenhot ophiolitic complex: Implications for the tectonic evolution of the Inner Mongolia-Daxinganling Orogenic Belt. *J. Asian Earth Sci.* **2015**, *97*, 279–293. [[CrossRef](#)]
16. Badarch, G.; Cunningham, W.D.; Windley, B.F. A new terrane subdivision for Mongolia: Implications for the Phanerozoic crustal growth of Central Asia. *J. Asian Earth Sci.* **2002**, *21*, 87–110. [[CrossRef](#)]
17. Eizenhöfer, P.R.; Zhao, G.; Sun, M. Geochronological and Hf isotopic variability of detrital zircons in paleozoic strata across the accretionary collision zone between the north China craton and Mongolian arcs and tectonic implications. *Geol. Soc. Am. Bull.* **2015**, *65*, 487–508. [[CrossRef](#)]
18. Jahn, B.M.; Capdevila, R.; Liu, D.Y. Sources of Phanerozoic granitoids in the transect Bayanhongor-Ulaan Baatar, Mongolia: Geochemical and Nd isotopic evidence, and implications for Phanerozoic crustal growth. *J. Asian Earth Sci.* **2004**, *23*, 629–653. [[CrossRef](#)]
19. Khain, E.V.; Bibikova, E.V.; Salnikova, E.B. The Palaeo-Asian Ocean in the Neoproterozoic and Early Palaeozoic: New geochronologic data and palaeotectonic reconstructions. *Precambrian Res.* **2003**, *122*, 329–358. [[CrossRef](#)]
20. Li, S.C.; Wang, H.T.; Li, G.; Wang, X.; Yang, X.P.; Zhao, Z.R. Northward plate subduction process of the Paleo-Asian Ocean in the middle part of the Central Asian orogenic belt: Evidence from adakites. *Acta Petrol. Sinica* **2020**, *36*, 2521–2536.
21. Li, Y.J.; Wang, G.H.; Santosh, M.; Wang, J.F.; Dong, P.P.; Li, H.Y. Supra-subduction zone ophiolites from Inner Mongolia, North China: Implications for the tectonic history of the southeastern Central Asian orogenic belt. *Gondwana Res.* **2018**, *59*, 126–143. [[CrossRef](#)]
22. Jian, P.; Kröner, A.; Windley, B.F. Carboniferous and Cretaceous mafic-ultramafic massifs in Inner Mongolia (China): A SHRIMP zircon and geochemical study of the previously presumed integral “Hegenshan ophiolite”. *Lithos* **2012**, *142–143*, 48–66. [[CrossRef](#)]
23. Miao, L.C.; Fan, W.M.; Liu, D.Y.; Zhang, F.Q.; Shi, Y.R.; Guo, F. Geochronology and geochemistry of the Hegenshan ophiolitic complex: Implications for late-stage tectonic evolution of the Inner Mongolia-Daxinganling Orogenic Belt, China. *J. Asian Earth Sci.* **2008**, *32*, 348–370. [[CrossRef](#)]
24. Kröner, A.; Kovach, V.; Belousova, E. Reassessment of continental growth during the accretionary history of the Central Asian Orogenic Belt. *Gondwana Res.* **2014**, *25*, 103–125. [[CrossRef](#)]
25. Jahn, B.M.; Windley, B.; Natal' in, B.; Dobretsov, N. Phanerozoic continental growth in Central Asia. *J. Asian Earth Sci.* **2004**, *23*, 599–603. [[CrossRef](#)]
26. Shao, J.A.; Tian, W.; Tang, K.D.; Wang, Y. Petrogenesis and tectonic settings of the late carboniferous high-Mg basalts of Inner Mongolia. *Earth Sci. Front.* **2015**, *22*, 171–181.
27. Xu, W.L.; Hergt, J.M.; Gao, S. Interaction of adakitic melt-peridotite: Implications for the high-Mg signature of Mesozoic adakitic rocks in the eastern North China Craton. *Earth Planet. Sci. Lett.* **2008**, *265*, 123–137. [[CrossRef](#)]
28. Wang, S.; Liu, Y. Geological and Mineral Survey Report on the Xiwuqi-Bainaimiao Areas of the Erlian Dongwuqi Metallogenic Belt. *Tianjin Geol. Surv. Cent. China Geol. Surv.* **2020**, 1–530.
29. Li, Y.J.; Wang, J.F.; Wang, G.H. Discovery and significance of the Dahate fore-arc basalts from the Diyanmiao ophiolite in Inner Mongolia. *Acta Petrol. Sin.* **2018**, *34*, 469–482.
30. Wang, J.; Li, Y.; Li, H. Discovery of the Late Carboniferous adakite in the Erenhot-Hegenshan suture zone and intra-oceanic subduction of the Paleo-Asian ocean. *Geol. China* **2021**, *48*, 520–535. (In Chinese with English Abstract)
31. Wang, J.; Li, Y.; Li, H. Late Carboniferous TTG magmatic event in the Hegenshan suture zone: Zircon U-Pb geochronology and geochemical constraints from the Huduge trondhjemite. *Acta Geol. Sin.* **2021**, *95*, 396–412.
32. Wang, J.; Li, Y.; Li, H. Late Carboniferous intraoceanic subduction of the Paleo-Asian Ocean: New evidences from the Zagayin high-Mg andesite in the Meilaotewula SSZ ophiolite. *Geol. Rev.* **2020**, *66*, 289–306.
33. Yang, Z.L.; Zhang, X.H.; Gao, Y.L. Late Carboniferous gabbro-granite suite from West Ujimqin of central Inner Mongolia: Petrogenesis and geodynamic implication. *Acta Petrol. Sin.* **2022**, *38*, 830–854.

34. Zhang, X.F.; Liu, J.L.; Feng, J.L. Geochronological and geochemical features of volcanic rocks of Dashizhai Formation in UralSutai of XilinHot, Inner Mongolia, and their geological significance. *Geol. Bull. China* **2016**, *35*, 766–775.
35. Li, H.; Zhou, Z.; Li, P. A Late Carboniferous-Early Permian Extensional Event in Xi UjimqinQi, Inner Mongolia: Evidence from Volcanic Rocks of Dashizhai Formation. *Geotecton. Metallog.* **2016**, *40*, 996–1013.
36. Fan, Y.; Li, T.; Xiao, Q. Zircon U-Pb Ages, Geochemical Characteristics of Late Permian Granite in West UjimqinBanner, Inner Mongolia, and Tectonic Significance. *Geol. Rev.* **2019**, *65*, 248–266.
37. Wu, Y.; Tian, Q.G.; Wang, Z.Q. The Early Carboniferous volcanic rocks in Engeriyinpeng area of Sonid Left Banner, Inner Mongolia: Discovery and its tectonic significance. *Geol. Bull. China* **2019**, *38*, 1170–1182.
38. Zhang, X.; Cheng, Y.; Li, Y. Zircon U-Pb dating and geochemistry of the Late Carboniferous hornblendite in Dong Ujimqi Inner Mongolia and its tectonic significance. *Acta Geol. Sin.* **2021**, *95*, 1495–1507.
39. Liu, J.; Chi, X.; Zhang, X. Geochemical Characteristic of Carboniferous Quartz-Diorite in the Southern Xiwuqi Area, Inner Mongolia and Its Tectonic Significance. *Acta Geol. Sin.* **2009**, *83*, 365–376.
40. Niu, X.; Liu, F.; Feng, G. Petrogenesis of the Late Silurian to Early Devonian potassic alkaline rocks on the northern margin of the North China Craton and their constraints on the tectonic evolution. *Acta Petrol. Sin.* **2021**, *40*, 835–858.
41. Huang, B.; Fu, D.; Li, S.C. The age and tectonic implications of the Hegenshan ophiolite in Inner Mongolia. *Acta Petrol. Sin.* **2016**, *32*, 158–176.
42. He, Y.; Xu, B.; Zhang, L.Y. Discovery of a Late Devonian retroarc foreland basin Mongolia and its tectonic implications. *Acta Petrol. Sin.* **2018**, *34*, 3071–3082.
43. Li, M.T.; Tang, J.; Wang, Z.W. Geochronology and geochemistry of the Early Carboniferous volcanic rocks in SonidZuoqi, Inner Mongolia: Implication for the Carboniferous tectonic evolution and crustal nature of the eastern Central Asia orogenic belt. *Acta Petrol. Sircica* **2020**, *36*, 799–819.
44. Li, B.; Shi, Y.; Yang, F. Middle Silurian-Late Devonian tectonic evolution in the eastern segment of the northern margin of the North China Plate: Evidence from magmatic rocks in Gongzhuling area. *Acta Petrol. Sircica* **2022**, *38*, 2364–2396.
45. Andersen, T. Correction of common lead in U-Pb analyses that do not report ²⁰⁴Pb. *Chem. Geol.* **2002**, *192*, 59–79. [[CrossRef](#)]
46. Ludwig, K.R. *Isoplot 3.00: A Geochronological Toolkit for Microsoft Excel*; Special Publication No.4; Berkeley Geochronology 608 Center: Berkeley, CA, USA, 2003; pp. 1–70.
47. Liu, Y.S.; Hu, Z.C.; Gao, S. In situ analysis of major and trace elements of anhydrous minerals by LA-ICP-MS without applying an internal standard. *Chem. Geol.* **2008**, *257*, 34–43. [[CrossRef](#)]
48. Liu, Y.S.; Gao, S.; Hu, Z.C. Continental and Oceanic Crust Re-cycling-induced Melt-Peridotite Interactions in the Trans-North China Orogen: U-Pb Dating, Hf Isotopes and Trace Elements in Zircons from Mantle Xenoliths. *J. Petrol.* **2010**, *51*, 537–571. [[CrossRef](#)]
49. Liu, Y.S.; Hu, Z.C.; Zong, K.Q. Reappraisal and refinement of zircon U-Pb isotope and trace element analyses by LA-ICP-MS. *Chin. Sci. Bull.* **2010**, *55*, 1535–1546. [[CrossRef](#)]
50. Middlemost, E.A.K. Naming materials in the magma/igneous rock system. *Earth-Sci. Rev.* **1994**, *37*, 215–224. [[CrossRef](#)]
51. Irvine, T.N.; Barager, W.R.A. A guide to the chemical classification of the common volcanic rocks. *Can. J. Earth Sci.* **1971**, *8*, 523–548. [[CrossRef](#)]
52. Boynton, W.V. Cosmochemistry of the Rare Earth Elements: Meteorite Studies. *Rare Earth Elem. Geochem.* **1984**, *2*, 63–114.
53. Sun, S.S.; Mc Donough, W.F. Chemical and isotopic systematics of oceanic basalts: Implications for mantle compositions and processes. *Geol. Soc. Lond. Spec. Publ.* **1989**, *42*, 313–345. [[CrossRef](#)]
54. Bureau of Inner Mongolia Geology. 1:200,000 Maodeng regional geological survey report. 1976; 1–184.
55. Institute of Inner Mongolia Autonomous Region Geological Survey. 1:250,000 Chaokewula regional geological survey report. 2008; 1–256.
56. Wu, F.Y.; Li, X.H.; Yang, J.H. Discussions on the petrogenesis of granites. *Acta Petrol. Sin.* **2007**, *23*, 1217–1238.
57. Chappell, B.W. Aluminium saturation in I- and S-type granites and the characterization of fractionated haplogranites. *Lithos* **1999**, *46*, 535–551. [[CrossRef](#)]
58. Watson, E.B. Zircon saturation in felsic liquids: Experimental results and applications to trace element geochemistry. *Contrib. Mineral. Petrol.* **1979**, *70*, 407–419. [[CrossRef](#)]
59. Watson, E.B.; Harrison, T.M. Zircon saturation revisited: Temperature and composition effects in a variety of crustal magma types. *Earth Planet. Sci. Lett.* **1983**, *64*, 295–304. [[CrossRef](#)]
60. King, P.L.; Chappell, B.W.; Allen, C.M. Are A-type granites the high-temperature felsic granites? Evidence from fractionated granites of the Wangrah Suite. *Aust. J. Earth Sci.* **2001**, *48*, 501–514. [[CrossRef](#)]
61. Whalen, J.B.; Currie, K.L.; Chappell, B.W. A-type granites: Geochemical characteristics, discrimination and petrogenesis. *Contrib. Mineral. Petrol.* **1987**, *95*, 407–419. [[CrossRef](#)]
62. Liu, C.; Chen, X.; Chen, P. Subdivision Discrimination Criteria and Genesis for A-Type Rock Suites. *Geol. J. China Univ.* **2003**, *9*, 573–591.
63. Pichavant, M.; Montel, J.M.; Richard, L.R. Apatite solubility in peraluminous liquids: Experimental data and an extension of the Harrison-Watson model. *Geochim. Cosmochim. Acta* **1992**, *56*, 3855–3861. [[CrossRef](#)]
64. Collins, W.J.; Beams, S.D.; White, A.J.R. Nature and origin of A-type granites with particular reference to Southeastern Australia. *Contrib. Mineral. Petrol.* **1982**, *80*, 189–200. [[CrossRef](#)]

65. Chappell, B.W.; White, A.J.R.; Wyborn, D. The importance of residual source material (restite) in granite petrogenesis. *J. Pet.* **1987**, *28*, 1111–1138. [[CrossRef](#)]
66. Kemp, A.I.S.; Hawkesworth, C.J.; Paterson, B.A.; Kinny, P.D. Episodic growth of the Gondwana supercontinent from hafnium and oxygen isotopes in zircon. *Nature* **2006**, *439*, 580–583. [[CrossRef](#)]
67. Kemp, A.I.S.; Hawkesworth, C.J.; Foster, G.L.; Paterson, B.A.; Woodhead, J.D.; Hergt, J.M.; Gray, C.M.; Whitehouse, M.J. Magmatic and crustal differentiation history of granitic rocks from Hf-O isotopes in zircon. *Science* **2007**, *315*, 980–983. [[CrossRef](#)] [[PubMed](#)]
68. Shao, J.A.; Zhang, L.L.; Zhou, X.H. A further study on the ophiolite in Hegenshan, Inner Mongolia. *Acta Petrol. Sin.* **2019**, *35*, 2864–2872.
69. Pearce, J.A.; Harris, N.B.W.; Tindle, A.G. Trace element discrimination diagrams for the tectonic interpretation of granitic rocks. *J. Petrol.* **1984**, *25*, 956–983. [[CrossRef](#)]
70. Profeta, L.; Ducea, M.N.; Chapman, J.B.; Paterson, S.R.; Gonzales, S.M.H.; Kirsch, M.; Petrescu, L.; DeCelles, P.G. Quantifying crustal thickness over time in magmatic arcs. *Sci. Rep.* **2016**, *5*, 17786. [[CrossRef](#)] [[PubMed](#)]
71. Tang, M.; Ji, W.Q.; Chu, X.; Wu, A.B.; Chen, C. Reconstructing crustal thickness evolution from europium anomalies in detrital zircons. *Geology* **2021**, *49*, 76–80. [[CrossRef](#)]
72. Zhu, Z.Y.; Campbell, I.H.; Allen, C.M.; Burnham, A.D. S-type granites: Their origin and distribution through time as determined from detrital zircons. *Earth Planet. Sci. Lett.* **2020**, *536*, 116140. [[CrossRef](#)]
73. Wang, J.; Li, Y.; Li, H.; Dong, P. The Asagetu shoshonitic volcanic rocks in the Hegenshan suture: Zircon LA-ICP-MS U-Pb ages, geochemical features and its tectonic significance. *Geol. Rev.* **2021**, *4*, 918–935.
74. Wang, J.F.; Li, Y.J.; Li, H.Y.; Dong, P.P. Zircon U-Pb dating of the Shijiangshan Late Jurassic-Early Cretaceous A-type granite in Xi Ujimqin Banner of Inner Mongolia and its tectonic setting. *Geol. Bull. China* **2018**, *37*, 382–396.
75. Guo, X.; Sun, H.; Dong, A.; Ren, J.; Xu, R.; Gao, B. The genesis and dating of the Early Permian granitic rock in the north of XilinHot, Inner Mongolia. *Geol. China* **2019**, *46*, 1396–1409. (In Chinese with English Abstract)
76. Yuan, J.; Ren, Y.; Jiang, Z.; Qu, Y.; Wei, H. Zircon U-Pb Dating and Geochemistry of Granites in Early Carboniferous in Maodeng of XilinHot, Inner Mongolia and Their Geological Implications. *Geoscience* **2017**, *6*, 1131–1145.
77. Pang, C.J.; Wang, X.C.; Wen, S.N.; Krapez, B.; Wang, Y.Y.; Liao, W. Petrogenesis of Late Carboniferous gabbroic intrusions in the Xilinhot region of Inner Mongolia: Products of partial melting of a hydrous mantle source in an intra-continental extensional setting. *Acta Petrol. Sin.* **2018**, *34*, 2956–2972.

Disclaimer/Publisher’s Note: The statements, opinions and data contained in all publications are solely those of the individual author(s) and contributor(s) and not of MDPI and/or the editor(s). MDPI and/or the editor(s) disclaim responsibility for any injury to people or property resulting from any ideas, methods, instructions or products referred to in the content.